Image of a quantum-corrected black hole without Cauchy horizons illuminated by a static thin accretion disk

Shilong Huang,[1,*] Jiawei Chen,[1,†] and Jinsong Yang[1,‡]

[1]School of Physics, Guizhou University, Guiyang 550025, China

Latest advances in effective quantum gravity propose a quantum-corrected black hole solution that avoids Cauchy horizons. In this paper, we study the image of the black hole and explore the influence of the quantum parameter ζ on its image. First, we investigate the influence of ζ on the event horizon, photon sphere, critical impact parameter, and innermost stable circular orbit associated with the black hole. We find that all these quantities exhibit an increase with increasing ζ. Meanwhile, we analyze the allowed range of ζ from both theoretical and observational perspectives. We then derive the photon trajectory equation and analyze briefly the behavior of the trajectories. A detailed analysis shows that as ζ increases, the photon trajectories near the event horizon undergo modifications. Finally, by plotting the optical appearance of the black hole under three emission models, we find that as ζ increases, the quantum-corrected black hole exhibits a larger shadow, along with a brightening of the bright rings and a reduction in the spacing between them near the critical impact parameter. Therefore, we can distinguish the quantum-corrected black hole from the Schwarzschild one by its unique optical appearance.

I. INTRODUCTION

Soon after the general relativity (GR) was proposed, it precisely explained the precession of Mercury's orbit [1] and successfully predicted phenomena like gravitational redshift, light deflection, and gravitational waves [2–4]. Research on light deflection later developed into studies of black hole (BH) shadows and optical appearances [5–15]. In 2015, gravitational waves–one of the key predictions of GR–were directly detected, providing strong evidence for the theory [16, 17]. Subsequently, in 2019, the Event Horizon Telescope (EHT) released the first image of the supermassive BH M87*, offering further direct confirmation of GR [18].

Although GR has been very successful at macroscopic scales, it also faces many problems, with one well-known issue being the singularity problem [19, 20]. Singularities cause physical quantities to diverge and create incomplete geodesics in spacetime, breaking causality [21]. To resolve singularities, physicists began modifying GR and introducing quantum mechanics into gravitational theories, and suggested some candidate theories of quantum gravity [22, 23].

As a highly regarded quantum gravity theory, loop quantum gravity (LQG) aims to quantize spacetime geometry in a background-independent, non-perturbative framework [24–27]. After decades of development, LQG has two main fields: the canonical formulation and the covariant formulation. The canonical approach uses Ashtekar-Barbero variables [28, 29], and performs canonical quantization on spatial slices [24–27]. It predicts discrete spatial geometry and explains the microscopic origin of BH entropy [30–37]. The covariant approach uses spin foams as fundamental dynamical units [38–42]. It provides a path integral description for four-dimensional spacetime quantum evolution. To explore quantum gravity effects, LQG is applied to symmetry-reduced models: loop quantum cosmology (LQC) and loop quantum BH (LQBH). LQC resolves the Big Bang singularity by a quantum bounce [43–47]. On the other hand, LQBH aims to resolve the BH singularities, and to explore how quantum effects influence horizons, internal structures, and final states [48–53].

In the effective theories resulting from LQBH, the issue of covariance arises. Recently, this issue has been successfully addressed by rigorously deriving the conditions for covariance in the spherically symmetric case [54, 55]. In these works, an effective Hamiltonian constraint that preserves covariance by meeting the covariance condition was derived to determine semiclassical quantum-corrected spacetimes. The two covariant quantum-corrected BH solutions proposed in [54] have been preliminarily explored in the shadows, optical appearances, and gravitational wave signatures [14, 56–58]. It turns out that the quantum parameter ζ may change the shadow radius, photon ring structure, and accretion disk brightness distribution. Specifically, a higher value of parameter ζ leads to a smaller shadow radius for the first quantum-corrected BH (denoted as BH-I), while the quantum parameter has weak effects on the optical appearance for the second quantum-corrected BH (BH-II) [14]. In [55], the third quantum-corrected BH solution has been proposed. In this BH solution, there are not Cauchy horizons, and thus the BH may be stable under perturbation. The aim of this paper is to investigate the optical properties of the third quantum-corrected BH.

The remainder of this paper is organized as follows. In Sec. II, we briefly review this quantum-corrected BH spacetime without Cauchy horizons, then calculate the radius of the photon sphere and critical impact parameter, then combine data from EHT observations of M87* and Sgr A* to constrain the range of the quantum parameter ζ. In Sec. III, we analyze photon trajectories and their dependence on ζ. In Sec. IV, we examine the quantum parameter's influence on three typical emission profiles from a thin accretion disk. Finally, we summarize the study in Sec. V. In this paper, we will use the geometric unit system, i.e., $G = c = 1$.

* gs.slhuang24@gzu.edu.cn
† gs.chenjw23@gzu.edu.cn
‡ Corresponding author; jsyang@gzu.edu.cn

II. THE QUANTUM-CORRECTED BLACK HOLE AND ITS PHOTON SPHERE

Recently, a new spherically symmetric quantum-corrected BH spacetime without Cauchy horizons that maintains general covariance was proposed in [55]. The line element of the spacetime reads

$$\mathrm{d}s^2 = -f^{(n)}(r)\mathrm{d}t^2 + \frac{1}{\mu(r)f^{(n)}(r)}\mathrm{d}r^2 + h(r)(\mathrm{d}\theta^2 + \sin^2\theta\mathrm{d}\varphi^2), \tag{2.1}$$

where

$$\begin{aligned} f^{(n)}(r) &= 1 - (-1)^n \frac{r^2}{\zeta^2}\arcsin\left(\frac{2M\zeta^2}{r^3}\right) - \frac{n\pi r^2}{\zeta^2}, \\ \mu(r) &= 1 - \frac{4M^2\zeta^4}{r^6}, \\ h(r) &= r^2. \end{aligned} \tag{2.2}$$

Here M stands for the ADM mass, n is an arbitrary integer, and ζ denotes the quantum parameter. It is easy to see that the metric returns to the Schwarzschild metric when $n = 0$ and ζ approaches zero. In the present paper, we focus on the case of $n = 0$. For notation simplicity, we take $\zeta = 0$ to represent the Schwarzschild case and rescale the physical quantities (such as r, ζ, M) into the dimensionless quantities (r/M, ζ/M, 1). The domain of the arcsin function in the line element is determined by

$$r \geq (2M\zeta^2)^{1/3} \equiv r_{\min}. \tag{2.3}$$

A detailed analysis shows that for the line element (2.1), there exist three different spacetime structures depending on the value of M, each of which contains a BH region [55]. It turns out that there is one real root of $f^{(0)}(r)$ with [55]

$$M > \frac{\zeta}{2}\left(\frac{2}{\pi}\right)^{3/2}. \tag{2.4}$$

In this case, the real root corresponds to the event horizon of the BH, denoted by $r = r_\mathrm{h}$. Equation (2.4) leads to

$$\frac{\zeta}{M} < 2\left(\frac{\pi}{2}\right)^{3/2} \cong 3.9374, \tag{2.5}$$

which provides a constraint on ζ/M for the existence of the event horizon from a theoretical point of view. In the present paper, we only consider the BH with M satisfying Eq. (2.4). The first image in Fig. 1 shows the r_h as the function with ζ/M.

For a timelike or null geodesic in a static and spherically symmetric spacetime with metric g_{ab}, one can always choose Schwarzschild-like coordinates such that $\theta = \pi/2$ along the geodesic. In this case, the geodesic always lies in the equatorial plane. Then we have [59, 60]

$$-\kappa = g_{ab}\left(\frac{\partial}{\partial\tau}\right)^a\left(\frac{\partial}{\partial\tau}\right)^b, \tag{2.6}$$

where τ represents the affine parameter, $(\partial/\partial\tau)^a$ denotes the vector filed tangent to the geodesic, and

$$\kappa = \begin{cases} 1, & \text{for timelike geodesic.} \\ 0, & \text{for null geodesic.} \end{cases} \tag{2.7}$$

We are interested in the photon trajectories near the quantum-corrected BH described by Eq. (2.1). Then, we obtain

$$\begin{aligned} 0 &= g_{00}\left(\frac{\mathrm{d}t}{\mathrm{d}\tau}\right)^2 + g_{11}\left(\frac{\mathrm{d}r}{\mathrm{d}\tau}\right)^2 + g_{22}\left(\frac{\mathrm{d}\theta}{\mathrm{d}\tau}\right)^2 + g_{33}\left(\frac{\mathrm{d}\varphi}{\mathrm{d}\tau}\right)^2 \\ &= -f^{(0)}(r)\left(\frac{\mathrm{d}t}{\mathrm{d}\tau}\right)^2 + \frac{1}{\mu(r)f^{(0)}(r)}\left(\frac{\mathrm{d}r}{\mathrm{d}\tau}\right)^2 + h(r)\left(\frac{\mathrm{d}\varphi}{\mathrm{d}\tau}\right)^2. \end{aligned} \tag{2.8}$$

In the quantum-corrected spacetime (2.1), the two Killing vector fields $(\partial/\partial t)^a$ and $(\partial/\partial\varphi)^a$ determine two conserved quantities [59, 60]

$$\begin{aligned} E &:= -g_{ab}\left(\frac{\partial}{\partial t}\right)^a\left(\frac{\partial}{\partial\tau}\right)^b = f^{(0)}(r)\frac{\mathrm{d}t}{\mathrm{d}\tau}, \\ L &:= g_{ab}\left(\frac{\partial}{\partial\varphi}\right)^a\left(\frac{\partial}{\partial\tau}\right)^b = h(r)\frac{\mathrm{d}\varphi}{\mathrm{d}\tau}, \end{aligned} \tag{2.9}$$

where E and L are the photon's energy and angular momentum, respectively. Combining Eqs. (2.8) and (2.9), we derive the photon trajectory equation as

$$\left(\frac{\mathrm{d}r}{\mathrm{d}\varphi}\right)^2 = h(r)^2\left(\frac{1}{b^2} - V_\mathrm{eff}(r)\right)\mu(r), \tag{2.10}$$

where $b \equiv L/E$ is the impact parameter, and

$$V_\mathrm{eff}(r) = \frac{f^{(0)}(r)}{h(r)} \tag{2.11}$$

denotes the effective potential of the photon.

We find that the main difference between trajectory equation (2.10) in the quantum-corrected spacetime and that in the Schwarzschild BH is the additional term $\mu(r)$, which modifies the radial metric by quantum geometry. The behavior of this function $\mu(r)$ for different values of ζ/M is illustrated in Fig. 2. We can see that when ζ/M is large, $\mu(r)$ decreases rapidly near the event horizon, which may affect photon trajectories. Subsequently, observing the function $\frac{\mathrm{d}\varphi}{\mathrm{d}r}$ in Fig. 3, we see that at $\zeta/M = 3.5$ the rate of change of φ with r is significantly greater than 1, indicating that photons may undergo special deflection near the event horizon due to the influence of the quantum parameter.

From Eq. (2.10), it is easy to see that the trajectory of photons is determined by the impact parameter and the effective potential. Among the trajectories of photons orbiting the BH, there exists a special type of photon orbit, namely, the unstable photon sphere orbit. Photons on the photon sphere, when perturbed, either fall into the BH or moves towards infinity. For the unstable photon sphere orbit, the effective potential of photons satisfies:

$$\begin{aligned} \left.\frac{\mathrm{d}V_\mathrm{eff}(r)}{\mathrm{d}r}\right|_{r=r_\mathrm{ph}} &= 0, \\ \left.\frac{\mathrm{d}^2V_\mathrm{eff}(r)}{\mathrm{d}r^2}\right|_{r=r_\mathrm{ph}} &< 0, \end{aligned} \tag{2.12}$$

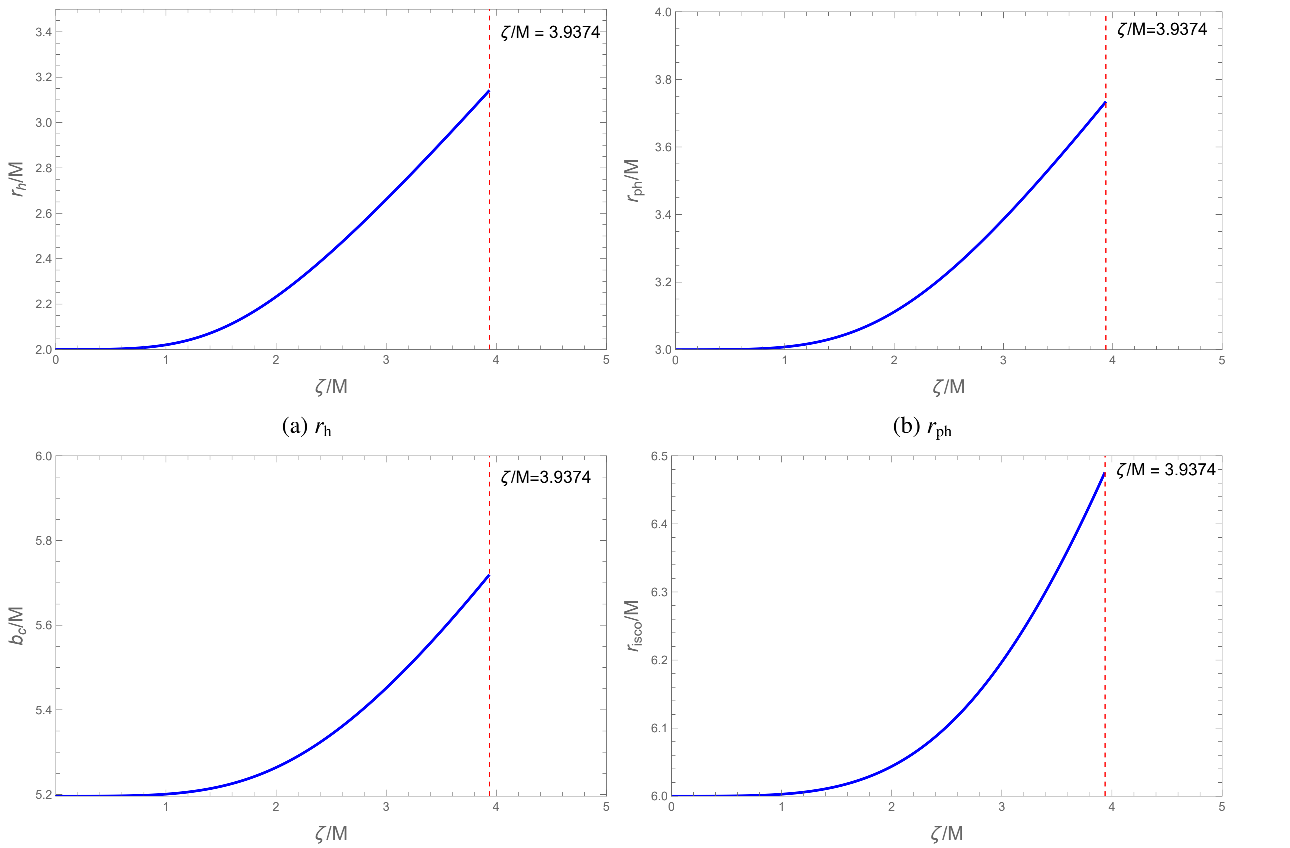

(a) r_{h} (b) r_{ph}

(c) b_{c} (d) r_{isco}

FIG. 1: The event horizon r_{h}, critical impact parameter b_{c}, radius of photon sphere r_{ph}, and innermost stable circular orbit r_{isco} as the functions of ζ/M. The vertical red dashed lines mark the location of the maximum allowed value $\zeta/M = 3.9374$.

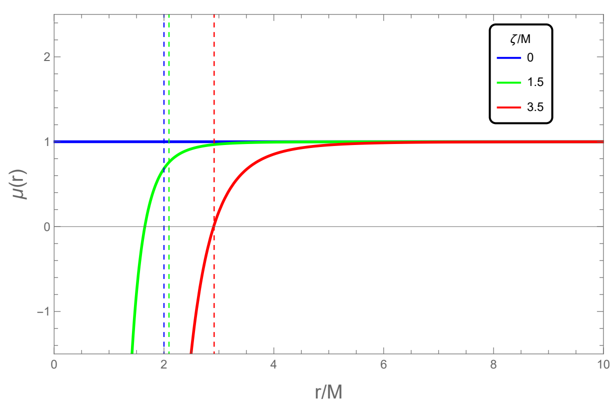

FIG. 2: Variation of $\mu(r)$ with radial coordinate r at three ζ/M values: 0 (blue), 1.5 (green), and 3.5 (red). The dashed lines mark where the event horizon forms for each ζ/M.

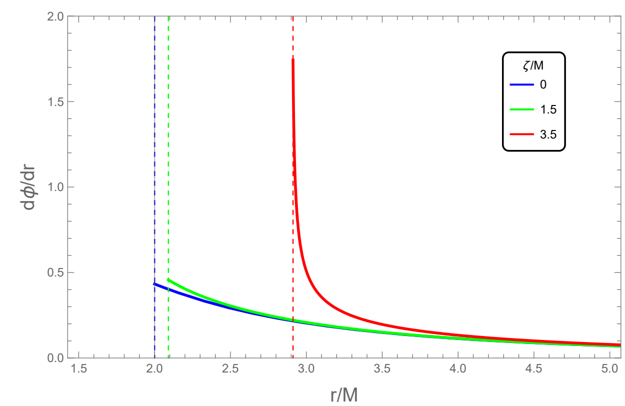

FIG. 3: Deflection rate $\frac{d\varphi}{dr}$ as a function of r for selected values of ζ/M: 0 (blue), 1.5 (green), and 3.5 (red). The dashed vertical lines indicate the event horizon for each case. The impact parameter is fixed at $b = b_{\mathrm{c}}/3$.

where r_{ph} is the radius of the photon sphere. The corresponding impact parameter is the critical impact parameter b_{c}, which satisfies:

$$V_{\mathrm{eff}}(r)\Big|_{r=r_{\mathrm{ph}}} = \frac{1}{b_{\mathrm{c}}^2}. \tag{2.13}$$

Given the value of the quantum parameter, we can calculate r_{ph} from Eq. (2.12), and then substitute the result into Eq. (2.13) to obtain the corresponding b_{c}. In panels (b) and (c) of Fig. 1, we show the dependence of both r_{ph} and b_{c} on

ζ/M. Their behavior exhibit patterns consistent with those of $r_{\rm h}$.

For the massive particle ($\kappa = 1$), we have

$$\left(\frac{\mathrm{d}r}{\mathrm{d}\varphi}\right)^2 = h(r)^2\left(\frac{\bar{E}^2}{\bar{L}^2} - \frac{f^{(0)}(r)}{\bar{L}^2} - \frac{f^{(0)}(r)}{h(r)}\right)\mu(r) \equiv \tilde{V}(r). \quad (2.14)$$

Here, $\bar{E}$ and $\bar{L}$ represent the energy and angular momentum of the massive particle, respectively. The innermost stable circular orbit (isco) for the massive particle is given by the following conditions [14, 61]:

$$\tilde{V}(r)\Big|_{r=r_{\rm isco}} = 0, \quad \frac{\mathrm{d}\tilde{V}(r)}{\mathrm{d}r}\Big|_{r=r_{\rm isco}} = 0, \quad \frac{\mathrm{d}^2\tilde{V}(r)}{\mathrm{d}r^2}\Big|_{r=r_{\rm isco}} = 0. \quad (2.15)$$

Thus, we obtain:

$$2\mu(r_{\rm isco})f^{(0)}(r_{\rm isco})\left[r_{\rm isco}\left(\frac{2f^{(0)\prime}(r_{\rm isco})}{f^{(0)}(r_{\rm isco})} - \frac{f^{(0)\prime\prime}(r_{\rm isco})}{f^{(0)\prime}(r_{\rm isco})}\right) - 3\right] = 0, \quad (2.16)$$

where the prime denotes the derivative with respect to r. Outside the event horizon, $f^{(0)}(r) > 0$ and $0 < \mu(r) \leq 1$. Hence, we have

$$r_{\rm isco} = \frac{3f^{(0)}(r_{\rm isco})f^{(0)\prime}(r_{\rm isco})}{2f^{(0)\prime}(r_{\rm isco})^2 - f^{(0)}(r_{\rm isco})f^{(0)\prime\prime}(r_{\rm isco})}. \quad (2.17)$$

The panel (d) in Fig. 1 shows the behavior of $r_{\rm isco}$ as the function of ζ/M. We can see from Fig. 1 that these four physical quantities ($r_{\rm h}$, $b_{\rm c}$, $r_{\rm ph}$, $r_{\rm isco}$) all increase monotonically with ζ/M.

While a theoretical constraint on ζ/M has been previously established in Eq. (2.5), to verify whether the theoretically derived constraint is consistent with the observational constraints, it is necessary to derive its observational bounds from the observational data, e.g., the EHT data. The angular diameter $\theta_{\rm d}$ of a BH shadow, as seen by a distant observer, is given by [62]

$$\theta_{\rm d} = 2\frac{b_{\rm c}}{D}, \quad (2.18)$$

where D is the distance from the observer to the BH. For M87*, the mass of the BH is $M = 6.5 \times 10^9 M_\odot$, the distance is $D = 16.8$Mpc, and its observed angular diameter falls within 29.32 μas to 51.06 μas [63, 64]. For Sgr A*, its mass is $M = 4.0 \times 10^6 M_\odot$ with a distance of $D = 8.15$kpc, and its angular diameter measures $48.7 \pm 7\,\mu$as [65]. Figure 4 presents the observational constraints on ζ/M for the quantum-corrected BH, derived from EHT observations of M87* and Sgr A*. The analysis yields the following upper limits: $\zeta/M \leq 6.6761$ for M87* and $\zeta/M \leq 4.0241$ for Sgr A*. The upper limits from both sets of observational data are higher than that of the theoretical constraint. Therefore, in the subsequent study, we restrict the quantum parameter to the range of $\zeta/M < 3.9374$.

III. PHOTON TRAJECTORIES

In this section, we investigate the photon trajectories around the quantum-corrected BH. We consider a quantum-corrected BH surrounded by a geometrically and optically thin, static accretion disk in its equatorial plane following Ref. [8]. Near the BH, light rays with different impact parameters may intersect the accretion disk an arbitrary number of times before ultimately falling into the BH or escaping to infinity. Therefore, it is reasonable to classify these light rays based on the number of times they intersect the thin accretion disk. This number is directly related to the total change in the photon's azimuthal angle [5, 8]. Thus, we first calculate this total change in azimuthal angle.

The total shift in the azimuthal angle is determined by Eq. (2.10). By employing the substitution $u = 1/r$, Eq. (2.10) is simplified as [9, 12, 59, 60]

$$\left(\frac{\mathrm{d}u}{\mathrm{d}\varphi}\right)^2 = G(u), \quad (3.1)$$

where

$$G(u) = \left[\frac{1}{b^2} - f^{(0)}\left(\frac{1}{u}\right)u^2\right]\left(1 - 4M^2\zeta^4u^6\right). \quad (3.2)$$

Then, the total change in azimuthal angle is given by [8, 9]

$$\varphi = \begin{cases} 2\displaystyle\int_0^{u_{\rm max}} \frac{\mathrm{d}u}{\sqrt{G(u)}}, & b > b_{\rm c}, \\ \infty, & b = b_{\rm c}, \\ \displaystyle\int_0^{u_{\rm h}} \frac{\mathrm{d}u}{\sqrt{G(u)}}, & b < b_{\rm c}. \end{cases} \quad (3.3)$$

Here, we introduce the notation $u_{\rm max} \equiv 1/r_{\rm min}$ to denote the inverse of the radial coordinate at the point of closest approach relative to the BH (i.e., the turning point) of photon trajectories with $b > b_{\rm c}$, which corresponds to the minimally positive real root of $G(u) = 0$. In addition, we define $u_{\rm h} \equiv 1/r_{\rm h}$ as the inverse of the horizon radius [9]. Using the classification scheme from Ref. [8], we define the total number of orbits as $n = \frac{\varphi}{2\pi}$. As a function of the impact parameter b, it satisfies:

$$n(b) = \frac{2m-1}{4}, \qquad m = 1, 2, 3, \cdots, \quad (3.4)$$

where m represents the number of intersections with the accretion disk. Therefore, for $1/4 < n < 3/4$, light rays cross the accretion disk once; for $3/4 < n < 5/4$, they intersect it at most two times; and for $n > 5/4$, they intersect it at least three times. From Eq. (3.3), we can find that for a given n (which means given φ), there exist two corresponding values of b, meaning that Eq. (3.4) has two solutions, denoted by $b_m^\pm$ with $b_m^- < b_{\rm c}$ and $b_m^+ > b_{\rm c}$. Then, the light trajectories can be classified in terms of the value of n as the following types [9, 12]:

$$\begin{cases} \text{Direct:} & 1/4 < n < 3/4 \Rightarrow b \in \left(b_1^-, b_2^-\right) \cup \left(b_2^+, \infty\right), \\ \text{Lensed:} & 3/4 < n < 5/4 \Rightarrow b \in \left(b_2^-, b_3^-\right) \cup \left(b_3^+, b_2^+\right), \\ \text{Photon ring:} & n > 5/4 \qquad\quad \Rightarrow b \in \left(b_3^-, b_3^+\right). \end{cases} \quad (3.5)$$

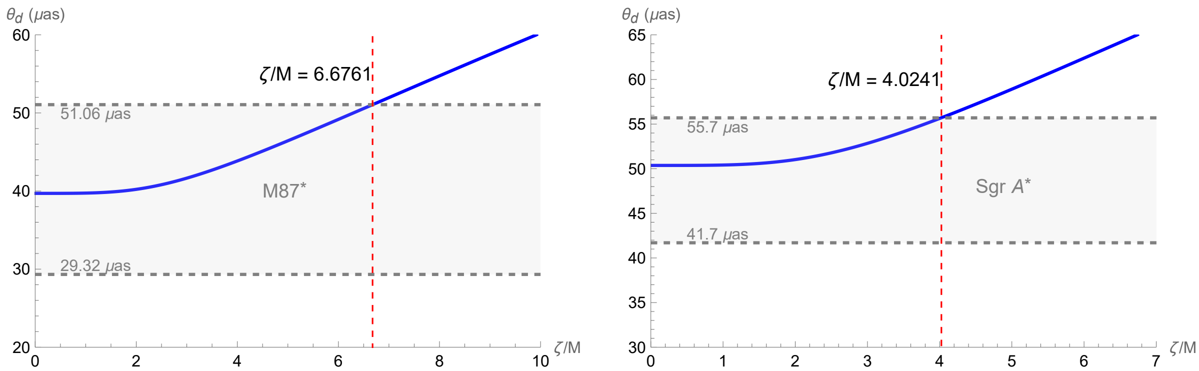

FIG. 4: Constraints on ζ/M from EHT observations of the shadow sizes for M87* (left) and Sgr A* (right). The gray areas show the observed diameters, and the red dashed lines mark the maximum allowed ζ/M.

TABLE I: Various physical quantities for the Schwarzschild BH and quantum-corrected BH, computed at multiple values of ζ/M.

ζ/M	r_h/M	r_{ph}/M	r_{isco}/M	b_c/M	b_1^-/M	b_2^-/M	b_2^+/M	b_3^-/M	b_3^+/M
0	2	3	6	5.19615	2.84770	5.01514	6.16757	5.18781	5.22794
1.5	2.09107	3.03930	6.01417	5.21925	2.91010	5.05516	6.17283	5.21229	5.24839
3	2.66087	3.38599	6.19719	5.45128	3.28197	5.35475	6.24598	5.44892	5.46583
3.5	2.91215	3.56561	6.33077	5.58624	3.43718	5.50527	6.32499	5.58462	5.59701

Finally, we clearly show the relationship between the orbital number n and b in Fig. 5. Meanwhile, we tabulate the values of $b_m^{\pm}$ and the other four physical quantities obtained in the previous section for different values of ζ/M in Table I. We find that as ζ/M increases, the range of impact parameters corresponding to both the lensed and the photon ring emission region of the quantum-corrected BH decreases.

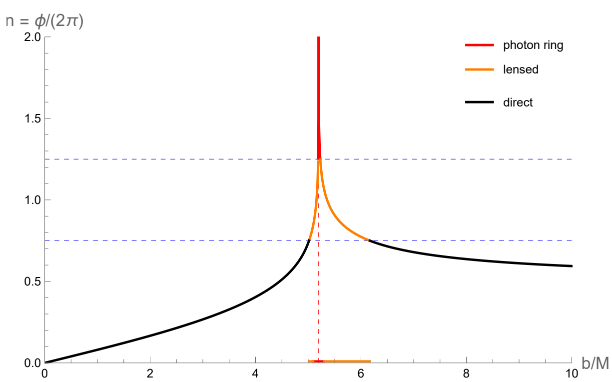

FIG. 5: Total number of orbits with $\zeta/M = 1.5$: $n < 3/4$ (black), $3/4 < n < 5/4$ (orange), and $n > 5/4$ (red), corresponding to the direct, lensed, and photon ring trajectories, respectively.

Based on the above classification, we employ the ray-tracing method to analyze the light rays traveling around the BH. Specifically, we use Eq. (2.10) to plot photon trajectories near the BH, as shown in Fig. 6. Visually, from the images, we observe that as ζ/M increases, both the photon sphere and the event horizon expand, and the distance between the photon sphere and the event horizon decreases. We quantitatively show this change in Fig. 7. Meanwhile, as ζ/M increases, the light rays gradually exhibit special deflection around the event horizon of the quantum-corrected BH, which is particularly evident in the image for $\zeta/M = 3.5$. Although Fig. 6 suggests that only light rays on the right side of the event horizon are affected, spherical symmetry implies that this influence occurs in all directions. We plot eight photon trajectories that are symmetric about the origin in Fig. 8 to illustrate this clearly.

IV. OPTICAL SIGNATURES OF THE BLACK HOLE WITH THIN DISK EMISSION

With the foundation laid in the preceding sections, we now turn to analyze the optical signatures of the quantum-corrected BH. To simplify, we consider that an observer is positioned at the north pole [8, 66]. The disk emits radiation with a specific intensity $I_\nu^{\rm em}(r)$, which in the local static frame depends only on the radial coordinate r and the emission frequency ν. As discussed previously, the number of times that photons intersect with the accretion disk is determined by their impact parameter b, and each intersection contributes to the total observed intensity. Thus, the overall observed intensity can be expressed as the sum of the intensities from each intersection [8]

$$I_{\rm obs}(b) = \sum_m f^{(0)}(r)^2 I_{\rm em}(r)\Big|_{r=r_m(b)}, \tag{4.1}$$

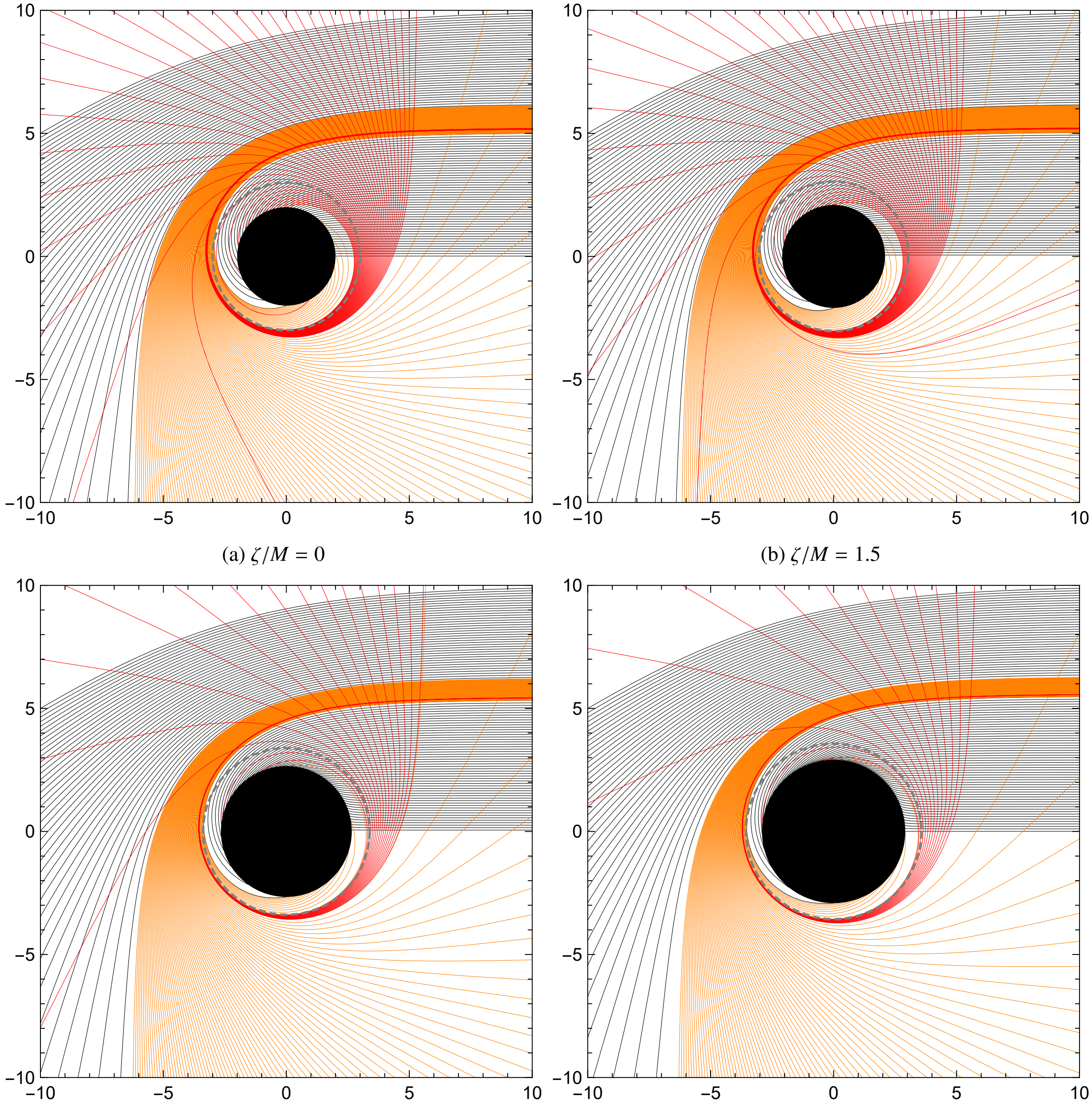

(a) $\zeta/M = 0$ (b) $\zeta/M = 1.5$

(c) $\zeta/M = 3$ (d) $\zeta/M = 3.5$

FIG. 6: Photon trajectories plotted against the impact parameter b for different quantum parameters. The black, orange, and red lines stand for the direct, lensed ring, and photon ring trajectories. A black disk shows the BH, and a dashed black curve marks the photon sphere.

where $I_{\rm em}(r) := \int I_\nu^{\rm em}(r)\mathrm{d}\nu$ is the total emitted intensity (integrated over all frequencies) at radius r. The function $r_m(b)$ is called the transfer function, which describes the radial coordinate r where a photon with an impact parameter b intersects the accretion disk for the m-th time. Hence, the first three transfer functions are defined as

$$\begin{cases} r_1(b) = \dfrac{1}{u\left(\frac{\pi}{2}, b\right)}, & b \in \left(b_1^-, \infty\right), \\ r_2(b) = \dfrac{1}{u\left(\frac{3\pi}{2}, b\right)}, & b \in \left(b_2^-, b_2^+\right), \\ r_3(b) = \dfrac{1}{u\left(\frac{5\pi}{2}, b\right)}, & b \in \left(b_3^-, b_3^+\right), \end{cases} \tag{4.2}$$

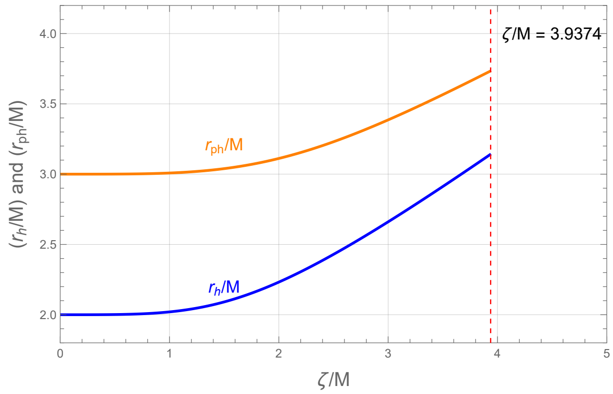

FIG. 7: Relative positions of the event horizon radius r_h (blue) and the photon sphere radius r_{ph} (orange), with the vertical red dashed line marking the location of the maximum allowed ζ/M.

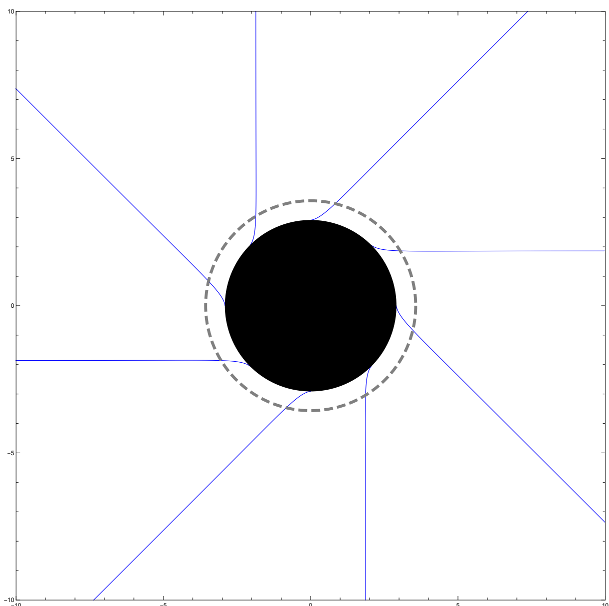

FIG. 8: Photon trajectories from different directions for $M = 1$ and $\zeta/M = 3.5$. The black disk shows the BH, and a dashed black curve marks the photon sphere.

where the function $u(\varphi, b)$ is obtained by solving the photon orbital equation (3.1). The behavior of the transfer functions $r_m(b)$ for the Schwarzschild BH is shown in Fig. 9. For $m = 1$, the rate of change dr_1/db is very close to 1. This term mainly produces the direct image of the accretion disk. It essentially reflects the redshift effect on the source profile distribution $I_{em}(r)$. For $m = 2$, dr_2/db increases rapidly. It corresponds to light rays that intersect the accretion disk of the BH at most twice (lensed ring). These rays form a highly demagnified and weak image. The image is confined to a much narrower range of b compared to the direct image. For $m = 3$, dr_3/db increases very quickly. It corresponds to light rays that intersect the accretion disk of the BH three times (photon ring). These rays form an extremely demagnified image confined to a very narrow range of b. The images produced by higher-order ($m > 3$) transfer functions are negligible due to their excessive demagnification [8].

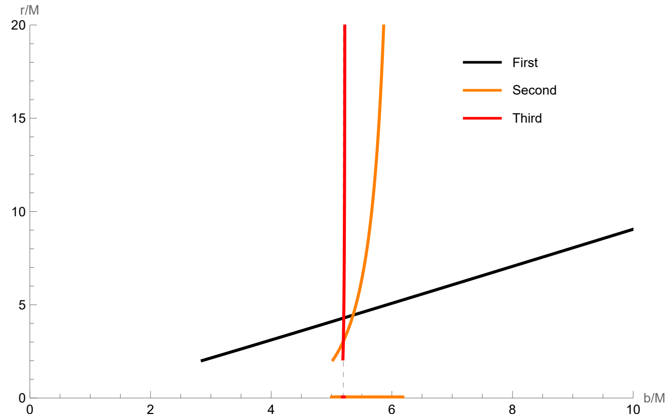

FIG. 9: The first three transfer functions for the Schwarzschild case. The black, orange, and red lines correspond to the first, second, and third transfer functions, respectively.

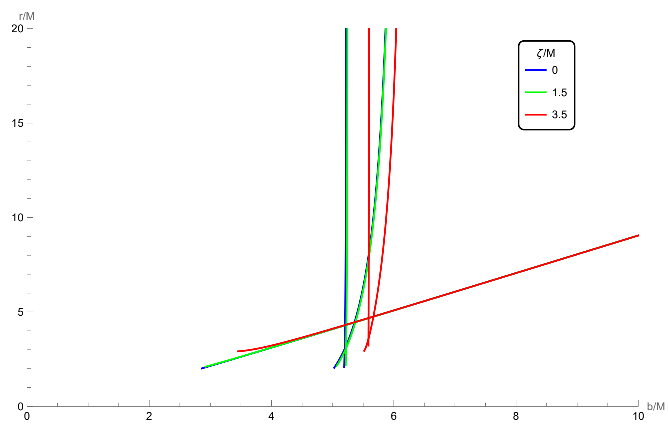

FIG. 10: The transfer functions of the quantum-corrected BH with $\zeta/M = 1.5$ (green) and $\zeta/M = 3.5$ (red) compared to those of the Schwarzschild BH with $M = 1$ (blue).

Moreover, Fig. 10 shows the transfer function images for the quantum-corrected BH with different values of ζ/M. Besides possessing some of the aforementioned similarities with the Schwarzschild case, we find that a large ζ/M significantly decreases the slope at the left end of the first transfer function. For the second transfer function, a similar behavior occurs at its left end, though this phenomenon is challenging to observe directly from Fig. 10. To clearly demonstrate this phenomenon, we present the slope image of the second transfer function in Fig. 11. The variation in the slope at the left end of the third transfer function is similar to that on the second transfer function.

To generate specific images, the emission intensity $I_{em}(r)$ from the disk should be specified. In the present paper, we consider the following three emission models [8, 66]:

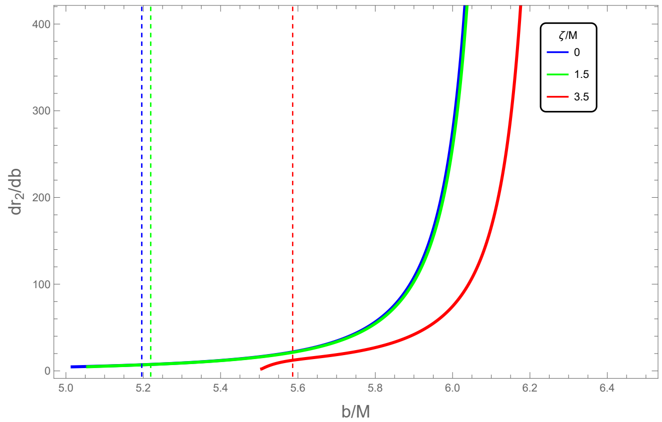

FIG. 11: Slope of the second transfer functions for the quantum-corrected BH with $\zeta/M = 1.5$ (green) and $\zeta/M = 3.5$ (red), and for the Schwarzschild BH (blue). The dashed lines mark the locations of b_c for these BHs.

- Model-I: Emission peaks at the $r_{\rm isco}$ and decays rapidly outward:

$$I_{\rm em}(r) := \begin{cases} I_0 \left[\dfrac{1}{r-(r_{\rm isco}-1)}\right]^2, & r > r_{\rm isco}, \\ 0, & r \le r_{\rm isco}. \end{cases} \tag{4.3}$$

- Model- II: Emission peaks at the $r_{\rm ph}$ and decays rapidly outward:

$$I_{\rm em}(r) := \begin{cases} I_0 \left[\dfrac{1}{r-(r_{\rm ph}-1)}\right]^3, & r > r_{\rm ph}, \\ 0, & r \le r_{\rm ph}. \end{cases} \tag{4.4}$$

- Model-III: Emission starts just outside the r_h and decays slowly outward:

$$I_{\rm em}(r) := \begin{cases} I_0 \dfrac{\frac{\pi}{2} - \arctan[r-(r_{\rm isco}-1)]}{\frac{\pi}{2} - \arctan[r_h-(r_{\rm isco}-1)]}, & r > r_h, \\ 0, & r \le r_h. \end{cases} \tag{4.5}$$

Here I_0 represents the peak emission intensity.

Figure 12 illustrates the emission intensities $I_{\rm em}/I_0$ for the three different emission models, while Fig. 13 shows the corresponding received intensity distributions and optical appearances as seen by a distant observer. Overall, compared to the Schwarzschild BH, the increase of ζ/M leads to a larger shadow for the quantum-corrected BH, a slight increase in the brightness of the bright rings, and a closer convergence of the two bright rings near b_c. Consequently, by comparing the shadow size, as well as the brightness and position of the bright rings, we can effectively distinguish the quantum-corrected BH from the Schwarzschild BH, as well as from BH-I and BH-II studied in Ref. [14].

V. SUMMARY

This paper presents a systematic study of the optical appearance of a quantum-corrected BH without Cauchy horizons illuminated by a static thin accretion disk. We first analyzed the influence of the quantum parameter on the event horizon radius r_h, the photon sphere radius $r_{\rm ph}$, the critical impact parameter b_c, and the innermost stable circular orbit $r_{\rm isco}$. As shown in Fig. 1, we found that all these quantities increase with ζ/M. We then constrain the parameter ζ/M from both theoretical and observational perspectives. Theoretically, to ensure the existence of an event horizon, ζ/M must be less than 3.9374; observationally, using EHT data on the shadow angular diameters of M87* and Sgr A*, we found that these two sets of data give the upper limits for ζ/M as 6.6761 and 4.0241, respectively, which are less restrictive than the theoretical bound.

Within the allowed parameter range, we further analyzed the trajectories of photons near the quantum-corrected BH, and found that as ζ/M increases, photon trajectories exhibit slight deflection near the event horizon as shown in Figs. 6 and 8.

Furthermore, we analyzed the the quantum gravity effects on the first three transfer functions, and found that when ζ/M is large, quantum correction influences the slope of the transfer functions, as shown in Fig. 11. Subsequently, combining the transfer functions, we investigated the optical appearance of the quantum-corrected BH under three typical emission profiles, and presented the results in Fig. 13. We found that a large ζ/M enlarges the shadow region, enhances the brightening of the bright rings, and converges the range between two bright rings. These features make the optical appearance of this quantum-corrected BH distinctly different from the Schwarzschild BH, BH-I, and BH-II.

In summary, our study reveals unique observational characteristics of the quantum-corrected BH, which can be used to distinguish it from the other BHs through future high-resolution radio observations (e.g., the next-generation EHT).

ACKNOWLEDGMENTS

This work is supported in part by NSFC Grants No. 12165005 and No. 11961131013.

[1] A. Einstein, Explanation of the perihelion motion of Mercury from the general theory of relativity. Sitzungsber. Preuss. Akad. Wiss. Berlin (Math. Phys.) **1915**, 831 (1915)

[2] A. Einstein and N. Rosen, On gravitational waves. J. Franklin Inst. **223**, 43 (1937). https://doi.org/10.1016/S0016-0032(37)90583-0

[3] P.C. Peters, Gravitational radiation and the motion of two point masses. Phys. Rev. **136**, B1224 (1964). https://doi.org/10.1103/

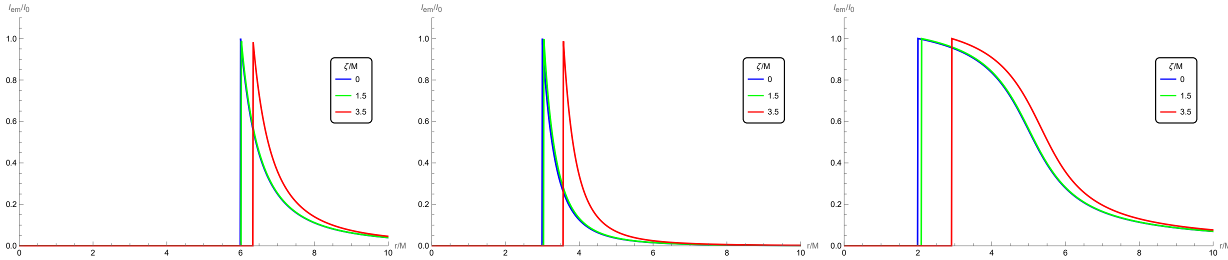

(a) Model-I (b) Model-II (c) Model-III

FIG. 12: Emission intensity profiles $I_{\rm em}(r)$ for the three models considered, shown for different values of ζ/M.

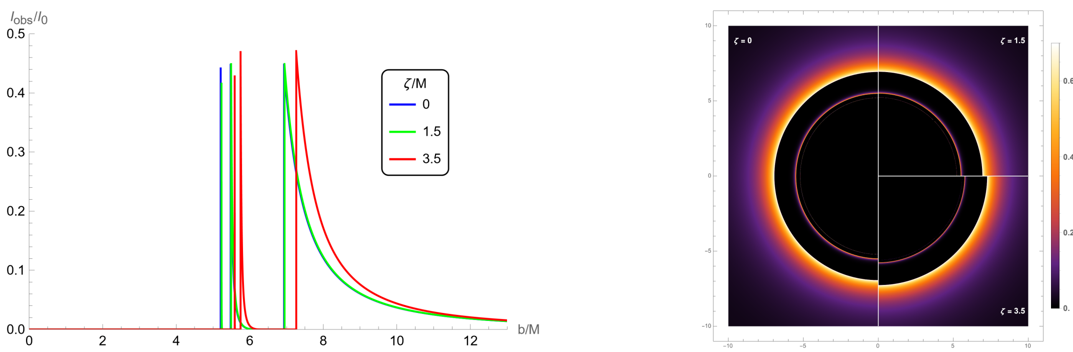

(a) Model-I (b) Optical-I.

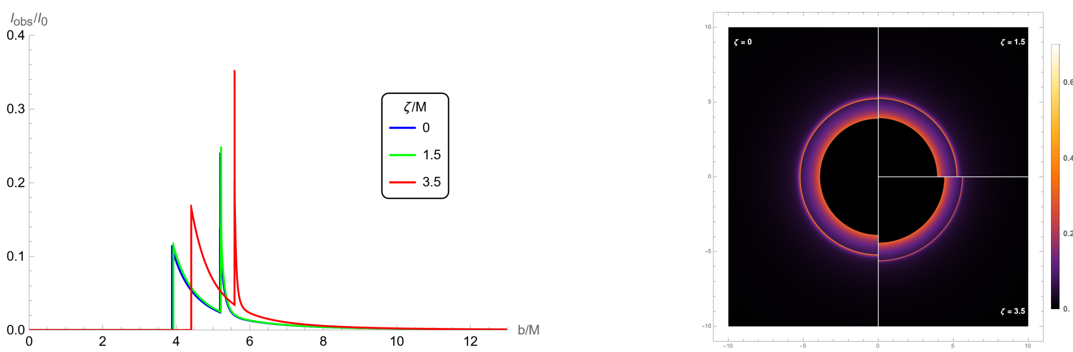

(c) Model-II (d) Optical-II.

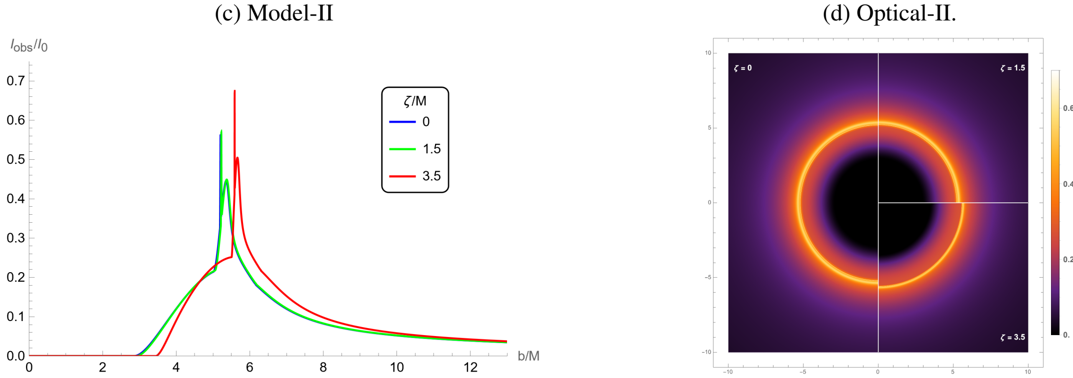

(e) Model-III (f) Optical-III.

FIG. 13: The observed intensity and visual structure of three accretion disks around a quantum-corrected BH under different ζ values. The left column shows the received intensity of this quantum-corrected BH. The right column includes images: the Schwarzschild BH (left), $\zeta/M = 1.5$ (upper right), and $\zeta/M = 3.5$ (lower right).

PhysRev.136.B1224
[4] H. Bondi, M.G.J. van der Burg, and A.W.K. Metzner, Gravitational waves in general relativity. VII. Waves from axisymmetric isolated systems. Proc. Roy. Soc. Lond. A **269**, 21 (1962). https://doi.org/10.1098/rspa.1962.0161
[5] J.P. Luminet, Image of a spherical black hole with thin accretion disk. Astron. Astrophys. **75**, 228 (1979)
[6] D.E. Holz and J.A. Wheeler, Retro-machos: π in the sky? Astrophys. J. **578**, 330 (2002). https://doi.org/10.1086/342463. arXiv:astro-ph/0209039
[7] K.S. Virbhadra and G.F.R. Ellis, Schwarzschild black hole lensing. Phys. Rev. D **62**, 084003 (2000). https://doi.org/10.1103/PhysRevD.62.084003. arXiv:astro-ph/9904193
[8] S.E. Gralla, D.E. Holz, and R.M. Wald, Black hole shadows, photon rings, and lensing rings. Phys. Rev. D **100**, 024018 (2019). https://doi.org/10.1103/PhysRevD.100.024018. arXiv:1906.00873
[9] J. Peng, M. Guo, and X.-H. Feng, Influence of quantum correction on black hole shadows, photon rings, and lensing rings. Chin. Phys. C **45**, 085103 (2021). https://doi.org/10.1088/1674-1137/ac06bb. arXiv:2008.00657
[10] Y. Hou, M. Guo, and B. Chen, Revisiting the shadow of braneworld black holes. Phys. Rev. D **104**, 024001 (2021). https://doi.org/10.1103/PhysRevD.104.024001. arXiv:2103.04369
[11] Y. Hou, Z. Zhang, H. Yan, M. Guo, and B. Chen, Image of a Kerr-Melvin black hole with a thin accretion disk. Phys. Rev. D **106**, 064058 (2022). https://doi.org/10.1103/PhysRevD.106.064058. arXiv:2206.13744
[12] J. Yang, C. Zhang, and Y. Ma, Shadow and stability of quantum-corrected black holes. Eur. Phys. J. C **83**, 619 (2023). https://doi.org/10.1140/epjc/s10052-023-11800-8. arXiv:2211.04263
[13] Z. Zhang, Y. Hou, M. Guo, and B. Chen, Imaging thick accretion disks and jets surrounding black holes. J. Cosmol. Astropart. Phys. **05**, 032 (2024). https://doi.org/10.1088/1475-7516/2024/05/032. arXiv:2401.14794
[14] J. Chen and J. Yang, Shadows and optical appearance of quantum-corrected black holes illuminated by static thin accretions. Eur. Phys. J. C **85**, 512 (2025). https://doi.org/10.1140/epjc/s10052-025-14230-w. arXiv:2503.06215
[15] J. Chen and J. Yang, Optical appearance of Schwarzschild black holes with optically thin and thick accretion disks at various inclination angles. arXiv:2506.22891
[16] B.P. Abbott *et al.* (LIGO Scientific Collaboration and Virgo Collaboration), Observation of Gravitational Waves from a Binary Black Hole Merger. Phys. Rev. Lett. **116**, 061102 (2016). https://doi.org/10.1103/PhysRevLett.116.061102. arXiv:1602.03837
[17] B.P. Abbott *et al.* (LIGO Scientific Collaboration and Virgo Collaboration), GW170817: Observation of Gravitational Waves from a Binary Neutron Star Inspiral. Phys. Rev. Lett. **119**, 161101 (2017). https://doi.org/10.1103/PhysRevLett.119.161101. arXiv:1710.05832
[18] K. Akiyama *et al.* (Event Horizon Telescope Collaboration), First M87 Event Horizon Telescope results. I. The shadow of the supermassive black hole. Astrophys. J. Lett. **875**, L1 (2019). https://doi.org/10.3847/2041-8213/ab0ec7. arXiv:1906.11238
[19] R. Penrose, Gravitational Collapse and Space-time Singularities. Phys. Rev. Lett. **14**, 57 (1965). https://doi.org/10.1103/PhysRevLett.14.57
[20] S.W. Hawking and R. Penrose, The Singularities of gravitational collapse and cosmology. Proc. Roy. Soc. Lond. A **314**, 529 (1970). https://doi.org/10.1098/rspa.1970.0021
[21] M.J. Cassidy and S.W. Hawking, Models for chronology selection. Phys. Rev. D **57**, 2372 (1998). https://doi.org/10.1103/PhysRevD.57.2372. arXiv:hep-th/9709066
[22] B.S. DeWitt, Quantum theory of gravity. I. The canonical theory. Phys. Rev. **160**, 1113 (1967). https://doi.org/10.1103/PhysRev.160.1113
[23] M. Reuter, Nonperturbative evolution equation for quantum gravity. Phys. Rev. D **57**, 971 (1998). https://doi.org/10.1103/PhysRevD.57.971. arXiv:hep-th/9605030
[24] C. Rovelli, *Quantum Gravity* (Cambridge University Press, Cambridge, England, 2004). https://doi.org/10.1017/CBO9780511755804
[25] T. Thiemann, *Modern Canonical Quantum General Relativity* (Cambridge University Press, Cambridge, England, 2007). https://doi.org/10.1017/CBO9780511755682. arXiv:gr-qc/0110034
[26] A. Ashtekar and J. Lewandowski, Background independent quantum gravity: A status report. Class. Quant. Grav. **21**, R53 (2004). https://doi.org/10.1088/0264-9381/21/15/R01. arXiv:gr-qc/0404018
[27] M. Han, Y. Ma, and W. Huang, Fundamental structure of loop quantum gravity. Int. J. Mod. Phys. D **16**, 1397 (2007). https://doi.org/10.1142/S0218271807010894. arXiv:gr-qc/0509064
[28] A. Ashtekar, New Variables for Classical and Quantum Gravity. Phys. Rev. Lett. **57**, 2244 (1986). https://doi.org/10.1103/PhysRevLett.57.2244
[29] J.F. Barbero G., Real Ashtekar variables for Lorentzian signature space times. Phys. Rev. D **51**, 5507 (1995). https://doi.org/10.1103/PhysRevD.51.5507. arXiv:gr-qc/9410014
[30] C. Rovelli and L. Smolin, Discreteness of area and volume in quantum gravity. Nucl. Phys. B **442**, 593 (1995). https://doi.org/10.1016/0550-3213(95)00150-Q. arXiv:gr-qc/9411005
[31] A. Ashtekar and J. Lewandowski, Quantum theory of geometry: I. Area operators. Class. Quant. Grav. **14**, A55 (1997). https://doi.org/10.1088/0264-9381/14/1A/006. arXiv:gr-qc/9602046
[32] A. Ashtekar and J. Lewandowski, Quantum theory of geometry II: Volume operators. Adv. Theor. Math. Phys. **1**, 388 (1997). https://doi.org/10.4310/ATMP.1997.v1.n2.a8. arXiv:gr-qc/9711031
[33] T. Thiemann, A length operator for canonical quantum gravity. J. Math. Phys. **39**, 3372 (1998). https://doi.org/10.1063/1.532445. arXiv:gr-qc/9606092
[34] Y. Ma, C. Soo, and J. Yang, New length operator for loop quantum gravity. Phys. Rev. D **81**, 124026 (2010). https://doi.org/10.1103/PhysRevD.81.124026. arXiv:1004.1063
[35] J. Yang and Y. Ma, New volume and inverse volume operators for loop quantum gravity. Phys. Rev. D **94**, 044003 (2016). https://doi.org/10.1103/PhysRevD.94.044003. arXiv:1602.08688
[36] A. Ashtekar, J. Baez, A. Corichi, and K. Krasnov, Quantum Geometry and Black Hole Entropy. Phys. Rev. Lett. **80**, 904 (1998). https://doi.org/10.1103/PhysRevLett.80.904. arXiv:gr-qc/9710007
[37] S. Song, H. Li, Y. Ma, and C. Zhang, Entropy of black holes with arbitrary shapes in loop quantum gravity. Sci. China Phys. Mech. Astron. **64**, 120411 (2021). https://doi.org/10.1007/s11433-021-1770-3. arXiv:2002.08869
[38] J.C. Baez, An introduction to spin foam models of *BF* theory and quantum gravity. Lect. Notes Phys. **543**, 25 (2000). https://doi.org/10.1007/3-540-46552-9_2. arXiv:gr-qc/9905087
[39] D. Oriti, Space-time geometry from algebra: Spin foam models for nonperturbative quantum gravity. Rept. Prog. Phys. **64**, 1703 (2001). https://doi.org/10.1088/0034-4885/64/12/203. arXiv:gr-qc/0106091
[40] A. Perez, Spin foam models for quantum gravity. Class. Quant.

Grav. **20**, R43 (2003). https://doi.org/10.1088/0264-9381/20/6/202. arXiv:gr-qc/0301113
[41] A. Perez, Introduction to loop quantum gravity and spin foams, in *2nd International Conference on Fundamental Interactions* (2004). arXiv:gr-qc/0409061
[42] A. Perez, The spin foam approach to quantum gravity. Living Rev. Rel. **16**, 3 (2013). https://doi.org/10.12942/lrr-2013-3. arXiv:1205.2019
[43] A. Ashtekar, M. Bojowald, and J. Lewandowski, Mathematical structure of loop quantum cosmology. Adv. Theor. Math. Phys. **7**, 233 (2003). https://doi.org/10.4310/ATMP.2003.v7.n2.a2. arXiv:gr-qc/0304074
[44] M. Bojowald, Loop quantum cosmology. Living Rev. Rel. **8**, 11 (2005). https://doi.org/10.12942/lrr-2005-11. arXiv:gr-qc/0601085
[45] A. Ashtekar, T. Pawlowski, and P. Singh, Quantum nature of the big bang: Improved dynamics. Phys. Rev. D **74**, 084003 (2006). https://doi.org/10.1103/PhysRevD.74.084003. arXiv:gr-qc/0607039
[46] Y. Ding, Y. Ma, and J. Yang, Effective Scenario of Loop Quantum Cosmology. Phys. Rev. Lett. **102**, 051301 (2009). https://doi.org/10.1103/PhysRevLett.102.051301. arXiv:0808.0990
[47] J. Yang, Y. Ding, and Y. Ma, Alternative quantization of the Hamiltonian in loop quantum cosmology. Phys. Lett. B **682**, 1 (2009). https://doi.org/10.1016/j.physletb.2009.10.072. arXiv:0904.4379
[48] M. Bojowald, Spherically symmetric quantum geometry: States and basic operators. Class. Quant. Grav. **21**, 3733 (2004). https://doi.org/10.1088/0264-9381/21/15/008. arXiv:gr-qc/0407017
[49] A. Ashtekar and M. Bojowald, Quantum geometry and the Schwarzschild singularity. Class. Quant. Grav. **23**, 391 (2006). https://doi.org/10.1088/0264-9381/23/2/008. arXiv:gr-qc/0509075
[50] L. Modesto, Semiclassical loop quantum black hole. Int. J. Theor. Phys. **49**, 1649 (2010). https://doi.org/10.1007/s10773-010-0346-x. arXiv:0811.2196
[51] R. Gambini, J. Olmedo, and J. Pullin, Spherically symmetric loop quantum gravity: Analysis of improved dynamics. Class. Quant. Grav. **37**, 205012 (2020). https://doi.org/10.1088/1361-6382/aba842. arXiv:2006.01513
[52] C. Zhang, Y. Ma, S. Song, and X. Zhang, Loop quantum Schwarzschild interior and black hole remnant. Phys. Rev. D **102**, 041502 (2020). https://doi.org/10.1103/PhysRevD.102.041502. arXiv:2006.08313
[53] X. Zhang, Loop quantum black hole. Universe **9**, 313 (2023). https://doi.org/10.3390/universe9070313. arXiv:2308.10184
[54] C. Zhang, J. Lewandowski, Y. Ma, and J. Yang, Black holes and covariance in effective quantum gravity. Phys. Rev. D **111**, L081504 (2025). https://doi.org/10.1103/PhysRevD.111.L081504. arXiv:2407.10168
[55] C. Zhang, J. Lewandowski, Y. Ma, and J. Yang, Black holes and covariance in effective quantum gravity: A solution without Cauchy horizons. Phys. Rev. D **112**, 044054 (2025). https://doi.org/10.1103/d6ks-d576. arXiv:2412.02487
[56] R.A. Konoplya and O.S. Stashko, Probing the effective quantum gravity via quasinormal modes and shadows of black holes. Phys. Rev. D **111**, 104055 (2025). https://doi.org/10.1103/PhysRevD.111.104055. arXiv:2408.02578
[57] W. Liu, D. Wu, and J. Wang, Light rings and shadows of static black holes in effective quantum gravity. Phys. Lett. B **858**, 139052 (2024). https://doi.org/10.1016/j.physletb.2024.139052. arXiv:2408.05569
[58] J. Chen and J. Yang, Periodic orbits and gravitational waveforms in quantum-corrected black hole spacetimes. Eur. Phys. J. C **85**, 726 (2025). https://doi.org/10.1140/epjc/s10052-025-14457-7. arXiv:2505.02660
[59] R.M. Wald, *General Relativity* (Chicago University Press, Chicago, 1984). https://doi.org/10.7208/chicago/9780226870373.001.0001
[60] C. Liang and B. Zhou, *Differential Geometry and General Relativity: Volume 1* (Springer, Singapore, 2023). https://doi.org/10.1007/978-981-99-0022-0
[61] X.-J. Wang, X.-M. Kuang, Y. Meng, B. Wang, and J.-P. Wu, Rings and images of Horndeski hairy black hole illuminated by various thin accretions. Phys. Rev. D **107**, 124052 (2023). https://doi.org/10.1103/PhysRevD.107.124052. arXiv:2304.10015
[62] R. Kumar and S.G. Ghosh, Rotating black holes in 4*D* Einstein-Gauss-Bonnet gravity and its shadow. J. Cosmol. Astropart. Phys. **07**, 053 (2020). https://doi.org/10.1088/1475-7516/2020/07/053. arXiv:2003.08927
[63] P. Kocherlakota *et al.* (Event Horizon Telescope Collaboration), Constraints on black-hole charges with the 2017 EHT observations of M87*. Phys. Rev. D **103**, 104047 (2021). https://doi.org/10.1103/PhysRevD.103.104047. arXiv:2105.09343
[64] X.-M. Kuang, Z.-Y. Tang, B. Wang, and A. Wang, Constraining a modified gravity theory in strong gravitational lensing and black hole shadow observations. Phys. Rev. D **106**, 064012 (2022). https://doi.org/10.1103/PhysRevD.106.064012. arXiv:2206.05878
[65] K. Akiyama *et al.* (Event Horizon Telescope Collaboration), First Sagittarius A* Event Horizon Telescope results. I. The shadow of the supermassive black hole in the center of the Milky Way. Astrophys. J. Lett. **930**, L12 (2022). https://doi.org/10.3847/2041-8213/ac6674. arXiv:2311.08680
[66] H.-M. Wang, Z.-C. Lin, and S.-W. Wei, Optical appearance of Einstein-Æther black hole surrounded by thin disk. Nucl. Phys. B **985**, 116026 (2022). https://doi.org/10.1016/j.nuclphysb.2022.116026. arXiv:2205.13174